Nonlinear Dyn
DOI 10.1007/s11071-006-9042-z

ORIGINAL ARTICLE

Friction-induced limit cycling in flexible rotor systems: An experimental drill-string set-up

N. Mihajlovic* · **N. van de Wouw** · **M. P. M. Hendriks** · **H. Nijmeijer**

Received: 20 April 2005 / Accepted: 14 July 2005

Abstract Friction-induced limit cycling deteriorates system performance in a wide variety of mechanical systems. In this paper, we study the way in which essential friction characteristics affect the occurrence and nature of friction-induced limit cycling in an experimental drill-string set-up. This study is performed on the level of a Lyapunov-based stability analysis and on the level of both numerical and experimental bifurcation analyses. The synthesis of these results confirms that friction-induced limit cycling is due to a subtle balance between negative damping at lower velocities and viscous friction at higher velocities. Moreover, it is shown how these essential friction characteristics depend on physical conditions such as temperature and normal forces in the frictional contact in the experimental set-up.

Keywords Discontinuous bifurcations · Experimental non-smooth dynamics · Flexible rotor systems · Friction-induced vibrations

*This work was performed while affiliated to the Eindhoven University of Technology.

N. Mihajlovic
Philips Research Laboratories, Prof. Holstlaan 4, 5656 AA Eindhoven, The Netherlands

N. van. de Wouw (✉) · M. P. M. Hendriks · H. Nijmeijer
Eindhoven University of Technology, Department of Mechanical Engineering, P.O. Box 513, 5600 MB Eindhoven, The Netherlands
e-mails: N.v.d.Wouw@tue.nl, M.P.M.Hendriks@tue.nl, H.Nijmeijer@tue.nl

1. Introduction

Friction-induced limit cycling endangers the performance and safety of operation of a wide range of mechanical systems. In this paper, we will focus on friction-induced limit cycling in mechanical systems with both friction and flexibilities. In this context, one can think of drilling rigs [1–3], printers, turbine blade dampers [4], industrial and domestic robots [5], simple earth-quake models, curve squealing of railway vehicles [6], accurate mirror positioning systems on satellites and many more. In these systems, the combination of friction and flexibility can give rise to limit cycling. This paper aims at revealing the dependency of such limit cycling on the friction characteristics through theoretical, numerical and experimental studies. In order to perform such experimental validation of the results, an experimental drill-string system is built in which both a flexibility and friction are present. This experimental set-up will support the study of friction-induced limit-cycling in general mechanical systems with friction and flexibilities and the study of friction-induced limit-cycling in drill-string systems in particular.

For the exploration and production of oil and gas, deep wells are drilled with a rotary drilling system. A rotary drilling system creates a borehole by means of a rock-cutting tool, called a bit. The torque driving the bit is generated at the surface by a motor with a mechanical transmission box. Via the transmission, the motor drives the rotary table: a large disc that acts as a kinetic energy storage unit. The medium to transport the energy

from the surface to the bit is a low-stiffness drill-string, mainly consisting of drill pipes. The lowest part of the drill-string is the Bottom-Hole-Assembly consisting of drill collars and the bit. The drill-string undergoes various types of vibrations during drilling: torsional (rotational) vibrations, caused by interaction between the bit and well, bending (lateral) vibrations, caused by pipe eccentricity, axial (longitudinal) vibrations, due to bouncing of the bit, and hydraulic vibrations in the circulation system, stemming from pump pulsations. Drill-string vibrations are an important cause for premature failure of drill-string components and drilling inefficiency. In this paper, torsional drill-string vibrations will be investigated. Drill rigs should generally operate at constant down-hole velocities (realised by a constant torque at the rotary table); therefore, the focus of this investigation will be on the steady-state behaviour of drill-string systems.

Extensive research on the subject of torsional vibrations has already been conducted [1–3, 7–9]. According to some of those results, the cause for torsional vibrations is the stick-slip phenomenon due to the friction force between the bit and the well [2, 8, 9]. Moreover, according to some other results, the cause for the torsional vibrations is negative damping in the friction force due to the contact between the bit and the borehole [1, 3]. In [10], it is stated that such a (effective) negative damping curve originates from the coupling between the axial and torsional dynamics in drill-string systems.

Friction-induced limit cycling is a performance limiting factor in many other types of mechanical systems. Survey papers on friction-induced limit cycling can be found in [11–14], in which specific friction characteristics are associated to the existence of such limit cycling. Moreover, in [15, 16] causes for friction-induced limit cycling, such as negative damping and fluctuating normal forces, are discussed. A limited amount of experimental work on friction-induced limit cycling in non-controlled systems is available [17]. It should be noted that friction-induced vibrations are also common in controlled mechanical systems, see [18–22].

In order to gain an improved understanding of the causes for torsional vibrations, an experimental drill-string set-up has been built. This experimental set-up consists of two discs, connected by a low-stiffness string. The upper disc is driven by a motor and at the lower disc a brake is implemented to exert a friction force on the disc. In this paper, we investigate along several routes how the occurrence and nature of the friction-induced vibrations depend on specific friction characteristics (of the friction exerted at the lower disc). Firstly, using a Lyapunov-based stability analysis the effect of certain friction characteristics on the stability of the desired constant-speed operating condition is studied. Secondly, an extensive numerical bifurcation analysis is performed for changing friction characteristics. Finally, such bifurcation analyses are also performed on an experimental level to confirm the validity of the model-based results. Moreover, physical conditions, such as temperature and normal forces applied to the brake, are changed in the experiments to illuminate the influence of such changes on the friction and the vibrations induced by the friction. The theoretical, numerical and experimental results jointly constitute a clear and coherent view on the way in which friction-induced limit cycles arise and change under changing frictional conditions.

In Section 2, the experimental set-up is introduced. The model of the set-up and the estimates for its parameters are discussed in Section 3. Section 4 discusses the dependency of the friction-induced limit cycling on specific friction characteristics on a model level; firstly through a theoretical stability analysis and secondly through numerical bifurcation analyses. In Section 5, the model-based results are compared to experimental results and the dependency of the occurrence of torsional vibrations on certain physical frictional conditions is investigated on an experimental level. Finally, Section 6 presents conclusions.

2. The experimental set-up

The experimental drill-string set-up is shown in Fig. 1. The set-up consists of a power amplifier, a DC-motor, two rotational (upper and lower) discs, a low-stiffness string and an additional brake applied to the lower disc. The input voltage from the computer is fed into the DC-motor via the power amplifier. The DC-motor is connected to the upper steel disc via the gear box, see Fig. 2. The upper disc and the lower disc are connected through a low-stiffness steel string. Both discs can rotate around their respective geometric centers and the related angular positions are measured using incremental encoders (see Fig. 2 for the encoder at the upper disc).

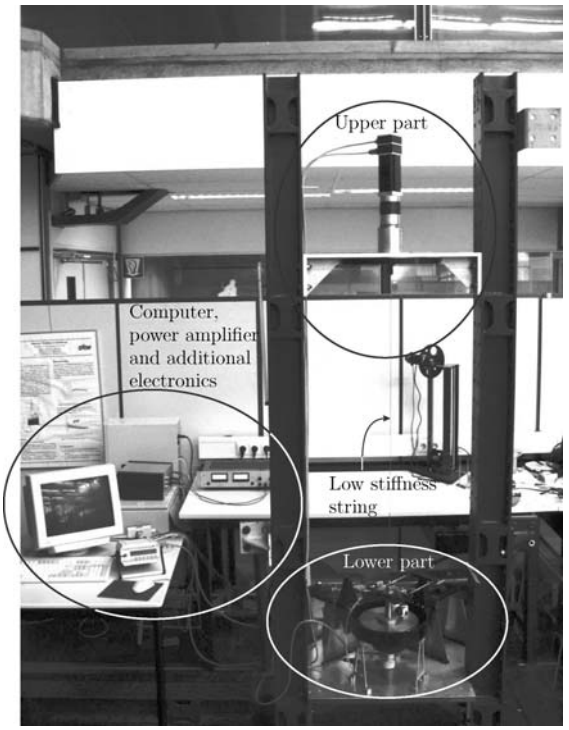

Fig. 1 Experimental drill-string set-up

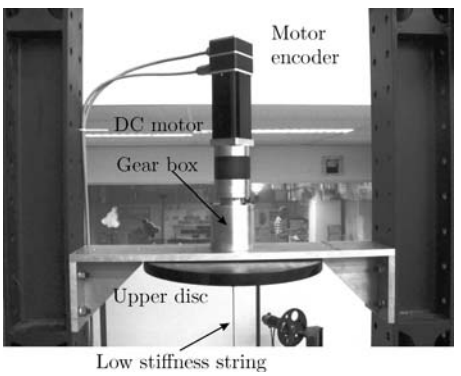

Fig. 2 The upper part of the experimental drill-string set-up

A brake and a small oil-box with felt stripes are fixed to the upper bearing housing of the lower part of the set-up, see Fig. 3. With the brake, a range of normal forces can be applied and the contact between the brake and the brake disc produces a friction force exerted on the brake disc. This friction force can induce torsional vibrations in the set-up. The brake contact material is bronze. The steel brake disc is connected to the lower brass disc via a very stiff shaft. The oil-box with the felt stripes is constructed in order to add oil (ondina oil 68) to the brake disc in a reproducible way. Namely, when liquid is present in the oil-box, the liquid is supplied to both sides of the brake disc by means of the capillary effect of the felt. This oil lubrication between the lower disc and the brake blocks will prove to be crucial for the existence of torsional vibrations in the set-up.

3. Model of the set-up

In this section, we introduce a dynamic model of the experimental drill-string set-up which will be used throughout the paper. The system is depicted schematically in Fig. 4.

By θ_u and θ_l we denote the angular displacements of the upper and lower disc, respectively. Moreover, $\omega_u = \dot{\theta}_u$ and $\omega_l = \dot{\theta}_l$ represent the angular velocities of the upper and lower disc, respectively. Furthermore, $\alpha = \theta_l - \theta_u$ represents the relative angular displacement of the lower disc with respect to the upper disc. In the sequel, we will use a state vector $\boldsymbol{x}$ defined by $\boldsymbol{x} = [\alpha \ \omega_u \ \dot{\alpha}]^T$. The equations of motion of the system are given by:

$$\begin{aligned} J_u\dot{\omega}_u - k_\theta\alpha + T_{fu}(\omega_u) &= k_m u, \\ J_A(\ddot{\alpha} + \dot{\omega}_u) + T_{fl}(\omega_u + \dot{\alpha}) + k_\theta\,\alpha &= 0, \end{aligned} \tag{1}$$

where J_u and J_A are the moments of inertia of respectively the upper and lower discs about their respective centers of mass, k_θ is the torsional spring stiffness, u is the input voltage to the motor and k_m is the motor constant. It should be noted that the friction torque at the upper disc $T_{fu}(\omega_u)$ is due to friction in the bearings of the upper disc and the electro-magnetic characteristic of the DC-motor [23, 24] and the friction torque at the lower disc $T_{fl}(\omega_l)$ comprises the friction in the bearings of the lower disc and the friction induced by the brake-mechanism. Both friction torques are modelled using set-valued force laws:

$$\begin{aligned} T_{fu}(\omega_u) &\in \begin{cases} T_{cu}(\omega_u)\mathrm{sgn}(\omega_u) & \text{for} \quad \omega_u \neq 0 \\ [-T_{cu}(0^-),\ T_{cu}(0^+)] & \text{for} \quad \omega_u = 0 \end{cases} \\ T_{fl}(\omega_l) &\in \begin{cases} T_{cl}(\omega_l)\mathrm{sgn}(\omega_l) & \text{for} \quad \omega_l \neq 0 \\ [-T_{cl}(0^-),\ T_{cl}(0^+)] & \text{for} \quad \omega_l = 0 \end{cases} \end{aligned}, \tag{2}$$

where the velocity dependency of the friction at the upper disc is expressed through $T_{cu}(\omega_u)$, with

$$T_{cu}(\omega_u) = T_{su} + \triangle T_{su}\mathrm{sgn}(\omega_u) + b_u|\omega_u| + \triangle b_u\omega_u, \tag{3}$$

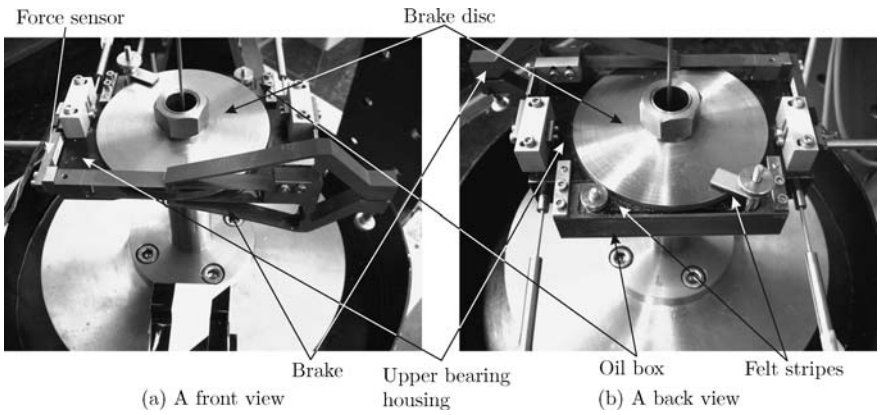

Fig. 3 The lower part of the set-up

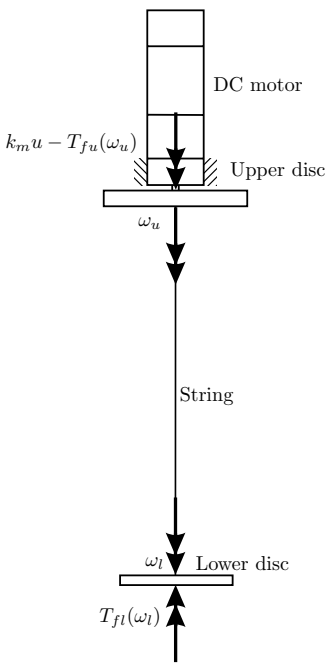

Fig. 4 Schematic representation of the drill-string set-up

and the velocity dependency of the friction at the lower disc is expressed through $T_{cl}(\omega_l)$, consisting of a Stribeck model with viscous friction:

$$T_{cl}(\omega_l) = T_{cl} + (T_{sl} - T_{cl})e^{-|\omega_l/\omega_{sl}|^{\delta_{sl}}} + b_l|\omega_l|. \qquad (4)$$

Equation (3) expresses the fact that we model the friction at the upper disc as a combination of dry friction and viscous friction and that it is asymmetric. Herein, $T_{cu}(0^+) = T_{su} + \triangle T_{su}$ and $-T_{cu}(0^-) = -T_{su} + \triangle T_{su}$ represent respectively the maximum and minimum value of the friction torque for zero angular velocities and $b_u + \triangle b_u$ and $b_u - \triangle b_u$ are viscous friction coefficients for positive and negative velocities, respectively. Equation (4) expresses the fact that the friction at the lower disc is modelled as a combination of dry friction and viscous friction, where the dry friction is described by a Stribeck curve for non-zero velocities. Herein, T_{cl} and T_{sl} represent the Coulomb friction and static friction levels, respectively, ω_{sl} is the Stribeck velocity, δ_{sl} the Stribeck shape parameter and b_l the viscous friction coefficient.

The parameters of the model are estimated using a nonlinear least-squares technique. For more information on the identification procedure and the validation results we refer to [24, 25]. Here, we summarise the result of this extensive identification procedure in Table 1. In the remainder of this paper, this parameter set will be referred to as the 'nominal' set of parameters. Especially the friction situation at the lower disc will be varied in order to investigate its influence on the friction-induced limit-cycling. Figure 5 shows the identified friction models, which indicate a pronounced Stribeck effect in the friction at the lower disc. It should be noted that here a normal force of 20.5 N is applied to the brake. Finally, the relatively small values of ΔT_{su} and Δb_u in Table 1 express the fact the friction model for the friction at the upper disc is close to symmetric.

4. Steady-state analysis of the dynamics

In this section, we study the steady-state behaviour of the drill-string system for constant values of the input voltage $u = u_c$ on a model level. Such steady-state behaviour is of particular interest in drill-string systems

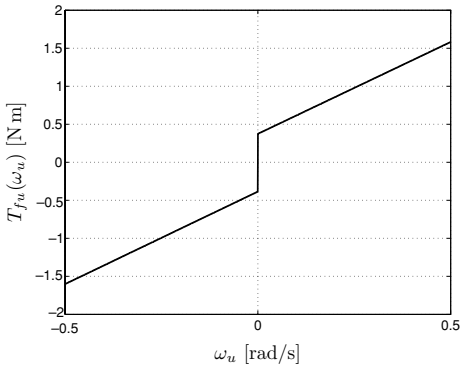

(a) Friction model at the upper disc.

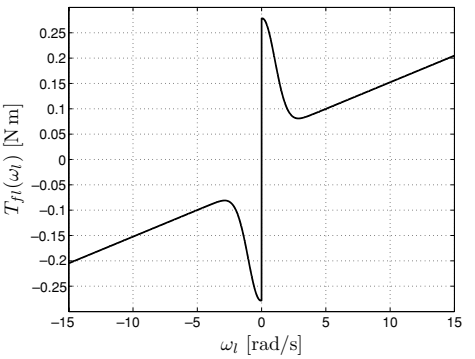

(b) Friction model at the lower disc.

Fig. 5 Estimated friction models

since these types of systems are generally driven by a constant torque while aiming at a constant velocity at the lower part of the system, because then drilling is most effective. Such constant-velocity condition reflects equilibria of (1). First, in Section 4.1 these equilibria, along with related stability properties, are discussed. In Section 4.2, the bifurcation diagram with the constant input voltage as a bifurcation parameter is presented for the friction model for the friction at the lower disc as introduced in Section 3 (the nominal case). Finally, in Section 4.3, the dependency of the steady-state behaviour on the friction characteristics at the lower disc is investigated.

4.1. Equilibria and related stability properties

The equilibria of the system, that correspond to a constant velocity of both discs, are investigated (Section 4.1.1) and the related local and global stability properties are presented depending on qualitative friction characteristics (Section 4.1.2). We only discuss the results for positive constant input voltages, since the results for negative input voltages are qualitatively comparable.

Table 1 Parameter estimates

Parameter		Estimated value
J_u	[kg m^2/rad]	0.4765
k_m	[Nm/V]	4.3228
T_{su}	[Nm]	0.37975
ΔT_{su}	[Nm]	−0.00575
b_u	[Nms/rad]	2.4245
Δb_u	[Nms/rad]	−0.0084
k_θ	[Nm/rad]	0.0775
J_A	[kg m^2/rad]	0.0414
T_{sl}	[Nm]	0.2781
T_{cl}	[Nm]	0.0473
ω_{sl}	[rad/s]	1.4302
δ_{sl}	[−]	2.0575
b_l	[Nms/rad]	0.0105

4.1.1. Equilibria

The equilibria $\boldsymbol{x}_{eq} = (\alpha_{eq}, \omega_{eq}, 0)$ of system (1), for $u = u_c$, with u_c a constant, satisfy the following equilibrium equations:

$$\begin{aligned} &T_{fl}(\omega_{eq}) + T_{fu}(\omega_{eq}) = k_m u_c, \\ &T_{fl}(\omega_{eq}) + k_\theta\, \alpha_{eq} = 0, \end{aligned} \tag{5}$$

which in fact represent algebraic inclusions due to the fact that both friction torques are modelled using the set-valued force laws (2). Let us now consider two cases:

1. equilibrium points for which $\omega_{eq} > 0$, i.e. both the lower and the upper disc rotate with the same constant angular velocity ω_{eq} and
2. equilibrium points for which $\omega_{eq} = 0$, i.e. both the lower and the upper disc stand still.

Let us first consider the case of $\omega_{eq} > 0$. For $\omega_{eq} > 0$, $T_{fu}(\omega_{eq}) = T_{cu}(\omega_{eq})$ and $T_{fl}(\omega_{eq}) = T_{cl}(\omega_{eq})$ (see (2)), where $T_{cu}(\omega_u)$ and $T_{cl}(\omega_l)$ are given by (3) and (4), respectively. Therefore, such

equilibrium points satisfy the following set of nonlinear algebraic equations

$$\begin{aligned} &k_m u_c - (T_{su} + \triangle T_{su}) - (b_u + \triangle b_u)\omega_{eq} \\ &\quad -T_{cl}(\omega_{eq}) = 0, \\ &\alpha_{eq} = -\frac{T_{cl}(\omega_{eq})}{k_\theta}. \end{aligned} \tag{6}$$

From (2), (4), the first algebraic equation of (6) and since $\omega_{eq} > 0$, it can be concluded that the system only exhibits such an isolated equilibrium point for

$$u_c > u_{\mathcal{E}} := \frac{T_{su} + \triangle T_{su} + T_{sl}}{k_m}. \tag{7}$$

This equation expresses the fact that the motor torque should overcome the joint static friction level at the upper and lower discs in order for the system to exhibit an equilibrium at non-zero velocity. In general, the first equation in (6) can have more than one solution. However, for the estimated parameters presented in Table 1, it holds that $-b_u - \triangle b_u - dT_{cl}/d\omega_l(\omega_l = \omega_{eq}) \leq 0, \ \forall\, \omega_{eq} > 0$, which means that the considered system has only one equilibrium point for a given $u_c > u_{\mathcal{E}}$ ($\omega_{eq} > 0$), taking into account (7). Clearly, the latter is mainly due to the relatively high viscous friction level at the upper disc.

Now, let us consider equilibria for $\omega_{eq} = 0$. Such equilibria only exist when the input voltage satisfies the condition: $0 \leq u_c \leq u_{\mathcal{E}}$. Moreover, (5) (with (2), (3) and (4)) implies that these equilibria constitute an equilibrium set $\mathcal{E}$, with

$$\mathcal{E} = \{x \in \mathbb{R}^3 \mid \dot{\alpha} = \omega_l = 0, \ \alpha \in [\alpha_{\min}, \ \alpha_{\max}]\}, \tag{8}$$

with

$$\begin{aligned} \alpha_{\min} &= \max\left(\frac{-k_m u_c - (T_{su} - \triangle T_{su})}{k_\theta}, \ -\frac{T_{sl}}{k_\theta}\right), \\ \alpha_{\max} &= \min\left(\frac{-k_m u_c + (T_{su} + \triangle T_{su})}{k_\theta}, \ \frac{T_{sl}}{k_\theta}\right). \end{aligned} \tag{9}$$

4.1.2. Stability of the equilibria

In the sequel, we investigate the (local and global) stability properties of these equilibria since the loss of such stability is strongly related to the occurrence of limit cycling. First we will address the stability properties of the isolated equilibrium points ($\omega_{eq} > 0$). The local stability properties can be accessed by means of linearisation. This yields the following condition for the local stability of these equilibrium points:

$$d_l := \left.\frac{\mathrm{d}T_{cl}}{\mathrm{d}\omega_l}\right|_{\omega_l = \omega_{eq}} > d_{\min} := \max\left(d_1, \ d_2, \ d_3\right), \tag{10}$$

where

$$\begin{aligned} d_1 &= -(b_u + \triangle b_u)J_A/J_u, \quad d_2 = -b_u - \triangle b_u \\ d_3 &= \frac{-J_u^2 k_\theta - (b_u + \triangle b_u)^2 J_A}{2\, J_u(b_u + \triangle b_u)} \\ &\quad + \frac{\sqrt{(J_u^2 k_\theta + (b_u + \triangle b_u)^2 J_A)^2 - 4\, J_u J_A^2 k_\theta (b_u + \triangle b_u)^2}}{2\, J_u(b_u + \triangle b_u)}. \end{aligned} \tag{11}$$

In other words, the local stability of these equilibria is guaranteed if the frictional damping at the lower disc at $\omega_u = \omega_l = \omega_{eq}$, denoted by d_l in (10), exceeds a certain threshold depending on the other system parameters as in (11). Therefore, it becomes immediately clear that a certain level of negative damping in $T_{cl}(\omega_l)$ can induce instability.

The global stability of the equilibria is assessed through a Lyapunov-based approach, see appendix A. Herein, a candidate Lyapunov function, defined by

$$\begin{aligned} V(\boldsymbol{x}, \boldsymbol{x}_{eq}) = &\frac{1}{2}k_\theta(\alpha - \alpha_{eq})^2 + \frac{1}{2}J_u(\omega_u - \omega_{eq})^2 \\ &+\frac{1}{2}J_A(\omega_u + \dot{\alpha} - \omega_{eq})^2 \end{aligned} \tag{12}$$

is used. The corresponding time-derivative of V equals

$$\begin{aligned} \dot{V}(\boldsymbol{x}, \boldsymbol{x}_{eq}) = &-(\omega_u - \omega_{eq})(T_{fu}(\omega_u) - T_{fu}(\omega_{eq})) \\ &-(\omega_u + \dot{\alpha} - \omega_{eq})(T_{fl}(\omega_u + \dot{\alpha}) \\ &-T_{fl}(\omega_{eq})). \end{aligned} \tag{13}$$

Consequently, a requirement on the negative semi-definiteness of $\dot{V}$ culminates in the following two incremental sector conditions for the friction at the upper disc and the friction at the lower disc:

$$-(\omega_u - \omega_{eq})(T_{fu}(\omega_u) - T_{fu}(\omega_{eq})) \leq 0 \tag{14}$$

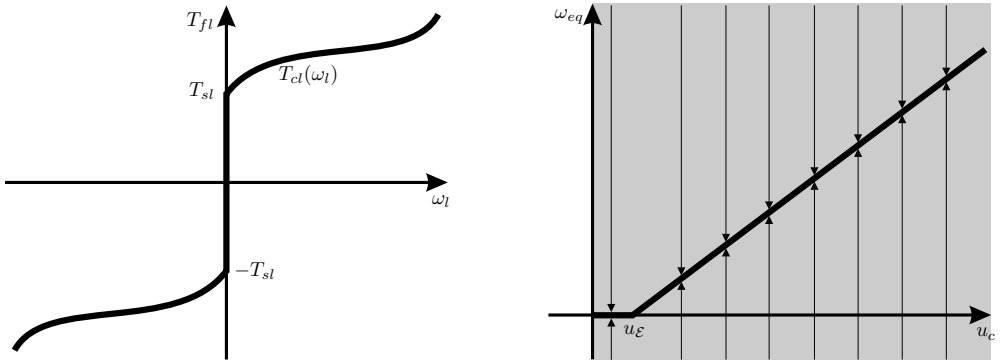

(a) Friction without negative damping. (b) Related stability properties.

Fig. 6 A friction model $T_{fl}(\omega_l)$ without negative damping and a graphical representation of stability properties of related equilibria

and

$$-(\omega_l - \omega_{eq})(T_{fl}(\omega_l) - T_{fl}(\omega_{eq})) \leq 0. \tag{15}$$

Considering the identified friction model at the upper disc, see Fig. 5(a), we can conclude that (14) is satisfied for all ω_u and ω_{eq}. However, (15) is not satisfied everywhere for the identified friction model at the lower disc, see Fig. 5(b), due to the fact that for a certain range of angular velocities of the lower disc a 'negative damping'-range is present.

The stability properties of the equilibrium set $\mathcal{E}$, for $u \leq u_{\mathcal{E}}$, are assessed using the same candidate Lyapunov function, see appendix A.

One of the main goals of this paper is to investigate the dependency of friction-induced limit-cycling on specific friction characteristics. Since the stability of the equilibria is crucial in this respect, these properties are studied for four types of (qualitatively different) friction models for the friction at the lower disc:

1. Consider a friction model $T_{fl}(\omega_l)$ which is a monotonically increasing function (see Fig. 6(a)). In Fig. 6(b), the equilibria of the system are depicted as far as the value of ω_{eq} is concerned with a constant input voltage u_c as a bifurcation parameter. Clearly, one can recognise that for $u_c < u_{\mathcal{E}}$ an equilibrium set, at which $\omega_{eq} = 0$, exists which condenses to an equilibrium point at $u_c = u_{\mathcal{E}}$ and progresses as a branch of isolated equilibria for increasing u_c. Due to the fact that no negative damping is present, the local stability of the isolated equilibria will be preserved for all u_c (see condition (10)). Moreover, even global asymptotic stability of both the equilibrium set and the isolated equilibria can be guaranteed since the incremental sector condition (15) on the friction model is always satisfied, see appendix A. These stability properties are schematically depicted in Fig. 6(b) by the arrows and a grey area spanning the entire range in vertical direction indicates global asymptotic stability.
2. Consider a friction model $T_{fl}(\omega_l)$ which exhibits a region of negative damping and a region of positive damping for very small and for very high velocities (a so-called humped friction model) as shown in Figs. 7(a) and (c). The essential difference between these two types of humped friction models lies in the fact that in Fig. 7(a), $\min(T_{cl}(\omega_l)) > T_{sl}$, and in Fig. 7(c), $\min(T_{cl}(\omega_l)) < T_{sl}$. In Fig. 7(b), the equilibria, and related stability properties, of the system with the friction model as in Fig. 7(a) are depicted. Based on the stability analyses, global stability (depicted by a grey area which extends along the entire vertical axis) and local stability (a bounded grey area in vertical direction) properties are displayed. The fact that local stability can not be guaranteed is caused by the fact that the isolated equilibria are unstable for $u_{h1} < u_c < u_{h2}$, where the subscript 'h' indicates that at these points Hopf bifurcations occur and u_{h1} and u_{h2} are defined by

$$u_{hi} = \frac{T_{cu}(\omega_{hi}) + T_{cl}(\omega_{hi})}{k_m}, \quad \text{with} \quad \left.\frac{\mathrm{d}T_{cl}}{\mathrm{d}\omega_l}\right|_{\omega_l=\omega_{hi}} = d_{\min}, \quad i = 1, 2, \tag{16}$$

see (10). Moreover, the global stability proof is limited by the satisfaction of the incremental

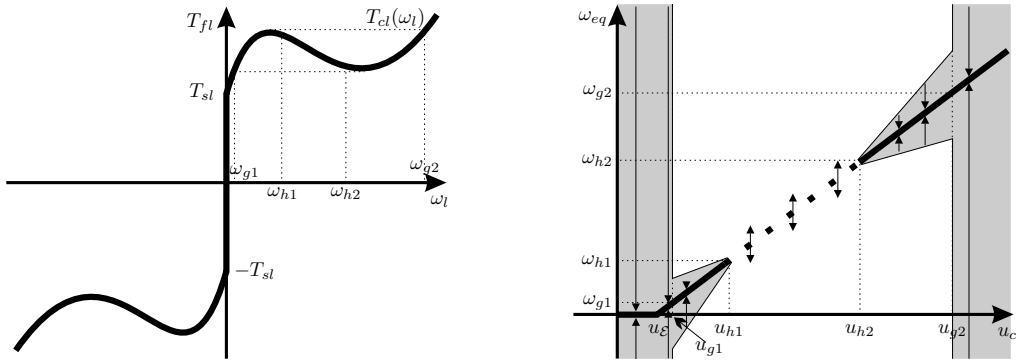

(a) A humped friction model.

(b) Related stability properties.

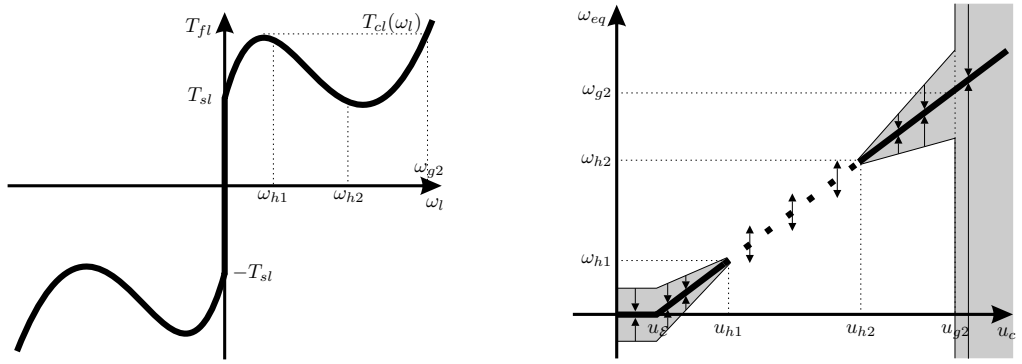

(c) A humped friction model.

(d) Related stability properties.

Fig. 7 Two types of humped friction models $T_{fl}(\omega_l)$ and a graphical representation of stability properties of related equilibria

sector condition (15), which is only satisfied for $u_c \in (0, u_{g1}) \cup (u_{g2}, \infty)$, where the subscript 'g' indicates that global stability can be guaranteed beyond these points and $u_{gi},\ i = 1, 2$, is defined by

$$u_{g1} = \frac{T_{cu}(\omega_{g1}) + T_{cl}(\omega_{g1})}{k_m},$$
$$u_{g2} = \frac{T_{cu}(\omega_{g2}) + T_{cl}(\omega_{g2})}{k_m}, \tag{17}$$

where ω_{g1} and ω_{g2} are chosen such that $T_{cl}(\omega_{g1}) = T_{cl}(\omega_2)$ and $T_{cl}(\omega_{g2}) = T_{cl}(\omega_1)$, respectively, with

$$\left.\frac{\mathrm{d}T_{cl}}{\mathrm{d}\omega_l}\right|_{\omega_l \in \{\omega_1,\, \omega_2\}} = 0,\ \omega_1 < \omega_2, \tag{18}$$

see Figs. 7 and 18. The fact that global stability is guaranteed for a significantly smaller range of input voltages than local stability is obviously due to the conservative nature of the Lyapunov-based stability analysis, but also hints towards the fact that limit cycling may exist for input voltages at which the equilibrium is locally stable, see Section 4.2. In Fig. 7(b) and (d), for $u_{h2} < u_c < u_{g2}$ the grey area increases for increasing u_c. This expresses the fact that for increasing u_c, the estimate of the region of attraction increases, see appendix A. The only difference between Figs. 7(b) and (d) is that in Fig. 7(d), we can not prove global asymptotic stability of the equilibrium set, which is caused by the fact that $\min(T_{cl}(\omega_l)) < T_{sl}$.

3. Consider a friction model $T_{fl}(\omega_l)$ which exhibits the Stribeck effect and positive damping exists only for high velocities (as shown in Fig. 8(a)). In this case, the isolated equilibrium points are globally asymptotically stable when $u_c \geq u_{g2}$. As far as the equilibrium set is concerned, we can only show that part of it is stable, see appendix A.

Figures 6–8 visualise the effect of friction characteristics on the stability of the equilibria, which is closely related to the occurrence or absence of limit cycling.

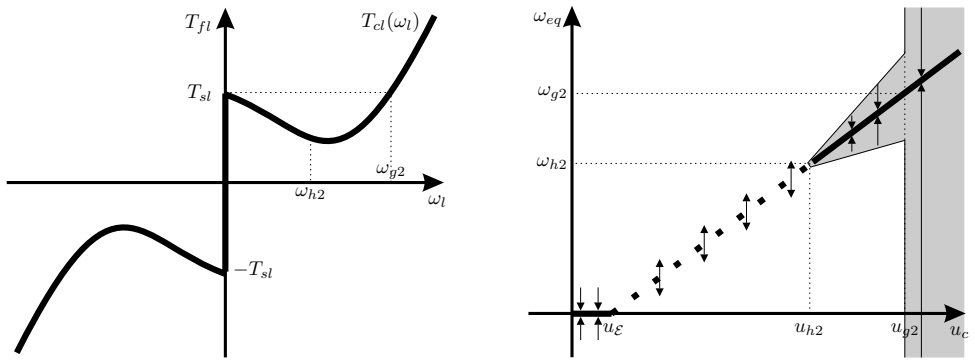

(a) Friction with a Stribeck effect. (b) Related stability properties.

Fig. 8 A friction model $T_{fl}(\omega_l)$ with a Stribeck effect and a graphical representation of stability properties of related equilibria

4.2. Bifurcation diagram (nominal case)

Here we analyze the steady-state behaviour (equilibria and limit cycles) of the estimated model, with parameters as in Table 1. More specifically, a bifurcation diagram with u_c as a bifurcation parameter is constructed. The equilibria are discussed in the previous section. According to the analysis in the previous section, Hopf bifurcation points occur for $u_c = u_{h1}$ and $u_c = u_{h2}$, which give rise to limit cycles. Using a path following technique in combination with a shooting method [26, 27], these limit cycles are computed numerically. Herein, the so-called switch model [28] is used to properly deal with the discontinuities in the dynamics, related to the set-valued nature of the friction models.

The results of an extensive bifurcation analysis are shown in a bifurcation diagram in Fig. 9, with u_c as a bifurcation parameter. In those figures, the maximal and minimal values of ω_l are plotted when a limit cycle is found. Floquet multipliers, corresponding to these limit cycles, are computed numerically and used to determine the local stability properties of these limit cycles. With respect to the obtained results, the following remarks can be made:

- For $u_c < u_\mathcal{E}$, an equilibrium set $\mathcal{E}$ exists indicated by branch e_1 which condenses to an equilibrium point at point A ($u_c = u_\mathcal{E}$) and progresses as an equilibrium branch e_2 of isolated equilibria.
- Point B ($u_c = u_{h1}$) represents a subcritical Hopf bifurcation point. For $u_c > u_{h1}$ an unstable equilibrium branch e_3 exists and an unstable periodic branch p_1 arises from point B, see Fig. 9(b). The periodic branch p_1 consists of limit cycles without stick-slip.
- The unstable periodic branch p_1 is connected to a locally stable periodic branch p_2 at the point(s) D, which represents a fold bifurcation point. Since the periodic branch p_2 consists of limit cycles which represent torsional vibrations with stick-slip, point D represents a discontinuous fold bifurcation. Fold bifurcations in Filippov systems are discussed in the references [28–30].
- Periodic branch p_2 consists only of locally stable limit-cycles with stick-slip, due to the non-smooth nonlinearities in the friction torque at the lower disc. For some higher constant input voltage u_c (point E in Fig. 9(a)) the locally stable periodic branch p_2 disappears through another discontinuous fold bifurcation. At this fold bifurcation point the stable periodic branch p_2 merges with an unstable periodic branch p_3.
- The unstable periodic branch p_3 is connected to the equilibrium branches e_3 and e_4 in the subcritical Hopf bifurcation point C.

It should be noted that the friction model in Fig. 5(b) corresponds to the type of friction model in Fig. 7(c). Consequently, the existence of the fold bifurcation point E is expected based on the analysis of global stability properties of equilibrium points (see Fig. 7(d)). Namely, the stability analysis for such friction model implies that the equilibrium points are locally asymptotically stable for $u_{h2} < u_c < u_{g2}$ and are globally asymptotically stable for $u_c > u_{g2}$, i.e. limit cycling can not persist beyond $u_c = u_{g2}$.

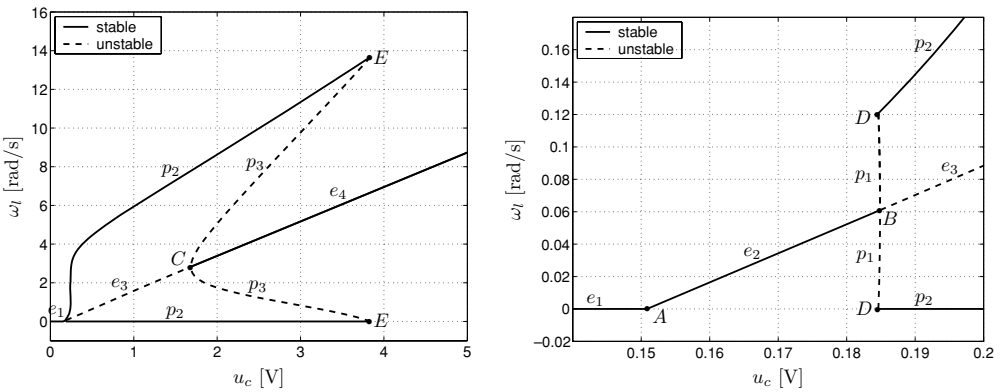

(a) The bifurcation diagram.

(b) Bifurcation diagram for small input voltages.

Fig. 9 Bifurcation diagram of system (1) with parameters as in Table 1

Consequently, $u_c = u_{g2}$ represents a (conservative) estimate of the voltage where the fold bifurcation point E occurs.

Summarizing, we can conclude that the instability which is induced by the negative damping in the friction gives rise to limit cycling. However, the range (in terms of u_c) for which limit cycling occurs is limited by the presence of viscous friction at higher angular velocities. Moreover, there exists a range of input voltages for which both stable equilibria and stable limit cycles exist. This co-existence can be explained by the fact that the viscous friction is only dominant in a neighborhood (in state-space) of the equilibria and outside this neighborhood the negative damping effect comes into plays once more giving rise to limit cycling. On this limit cycle a steady-state balance between the 'stabilizing' effect of viscous friction (at higher velocities) and the 'destabilizing' effect of negative damping (at lower velocities) is attained. In this respect, we should note that the magnitude of the range of input voltages for which such co-existence persists is directly related to the range of angular velocities $\omega_l \in [\omega_1, \omega_{g2}]$ (see Fig. 18), in which the friction force drops below its value for very low velocities (due to negative damping). Note that the magnitude of the range of angular velocities is determined by a balance between the level of negative damping and viscous friction. The fact that such subtle balance between negative damping and viscous friction is a crucial factor in the qualitative steady-state behaviour will be confirmed in the next section, in which the dependency of this behaviour on these friction characteristics is studied.

4.3. Changes in the friction characteristics

The previous sections show that the friction characteristics largely determine whether or not limit cycling occurs. Now, we will discuss the influence of these characteristics of the friction at the lower disc on the steady-state behaviour of the system. In doing so, we will use the friction model in Fig. 5(b) and the resulting bifurcation diagram, see Fig. 9, as a reference situation (i.e. the nominal case). The study of the stability of the equilibria in Section 4.1 shows that these stability properties are closely connected to two specific friction characteristics: firstly, the negative damping/Stribeck-effect and, secondly, the presence of viscous friction at higher velocities. Therefore, in this section we will explicitly investigate the influence of these two friction characteristics on the steady-state behaviour (i.e. on the bifurcation diagram).

4.3.1. Changes in the negative damping

In order to analyze the influence of various negative damping levels in $T_{fl}(\omega_l)$ on the steady-state behaviour of the drill-string system (1), we consider two friction situations that differ from the nominal case, see Fig. 10(a). In all cases, both the static friction level T_{sl} and the viscous friction coefficient b_l coincide with those of the nominal friction model. The angular velocities ω_{h1} and ω_{h2}, at which $d_l = d_{\min}$, are such that Hopf bifurcation points appear at approximately the same input voltages u_{h1} and u_{h2} (see expression (16) and Fig. 10(b)) as in the nominal case. However, in one friction situation the negative damping is higher

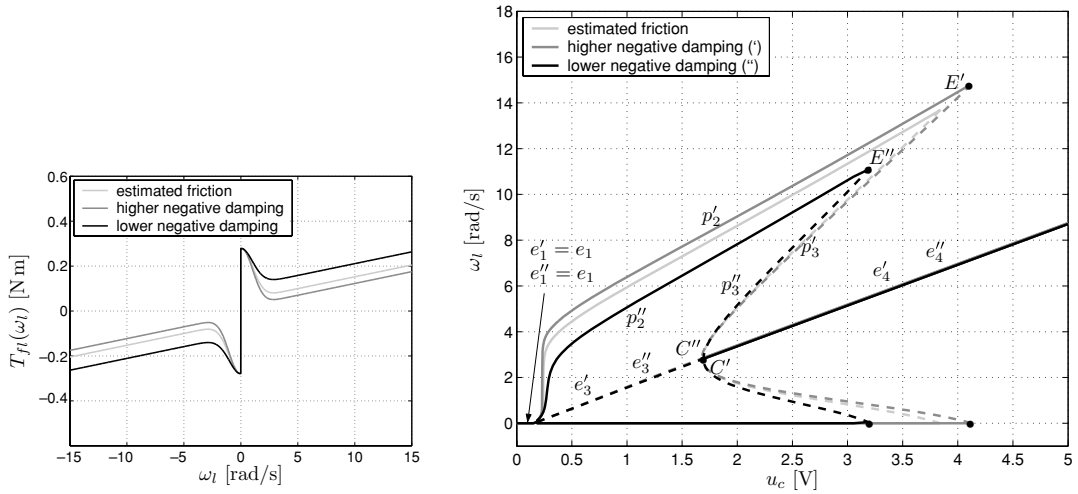

(a) Friction torques for various levels of negative damping.

(b) Bifurcation diagrams.

Fig. 10 Friction torques for various negative damping levels and related bifurcation diagrams

(dark-grey line in Fig. 10(a)) and in the second friction situation the negative damping is lower (black line in Fig. 10(a)) than in the nominal friction torque (light-grey line in Fig. 10(a)). The related bifurcation diagrams together with the bifurcation diagram for the nominal model are shown in Fig. 10(b).

When we compare these bifurcation diagrams the following can be concluded:

- Equilibrium branches e_1, e_1' and e_1'' are identical for all friction situations.
- The Hopf bifurcation points C, C' and C'' occur for (nearly) identical constant input voltages for all friction situations.
- If the negative damping is lower (black line in Fig. 10(a)), then torsional vibrations disappear for lower constant input voltages (compare discontinuous fold bifurcation points E' and E'' in Fig. 10(b)). In other words, if the negative damping in the friction torque at the lower disc is lower, then torsional vibrations appear for a smaller range of input voltages u_c. This can be explained using the analysis of the global stability properties of the equilibrium points performed in Section 4.1. In that section, we show that for $u_c > u_{g2}$ (u_{g2} is defined by (17) and Fig. 7(a)) equilibrium points of the system are globally asymptotically stable and, hence, no torsional vibrations can appear. We also conclude that u_{g2} does not represent the exact position of the fold bifurcation point, but only provides a conservative estimate of the constant voltage at which torsional vibrations disappear. If we determine u_{g2} for each friction situation shown in Fig. 10(a) we obtain that $u_{g2}' = 13.9890\,\mathrm{V}$ for the friction shown with dark-grey line and $u_{g2}'' = 9.2941\,\mathrm{V}$ for the friction shown with black line. Indeed, Fig. 10 shows that if the range of angular velocities defined by $\omega_l \in [\omega_1, \omega_{g2}]$ decreases (increases), due to a lower (higher) negative damping level, then the region (in terms of input voltages) of co-existence decreases (increases).
- From Fig. 10(b), we can conclude that a lower negative damping level causes lower amplitudes of the torsional vibrations in the drill-string system. Indeed, a lower negative damping level causes the friction force to be higher (see Fig. 10(a)), the dissipation of the energy due to such friction is higher, which in turn leads to a lower amplitude of the torsional vibrations.

4.3.2. Changes in the viscous friction

In order to discuss the influence of various viscous friction levels in $T_{fl}(\omega_l)$ on the steady-state behaviour of the drill-string system (1), we consider two friction situations in comparison with the nominal friction torque of the set-up, see Fig. 11(a). In all friction situations, the static friction level T_{sl} is the same and the friction torques differ only for high angular velocities ω_l. In one friction situation, the viscous friction level is higher (dark-grey line in Fig. 11(a)) and, in the second friction

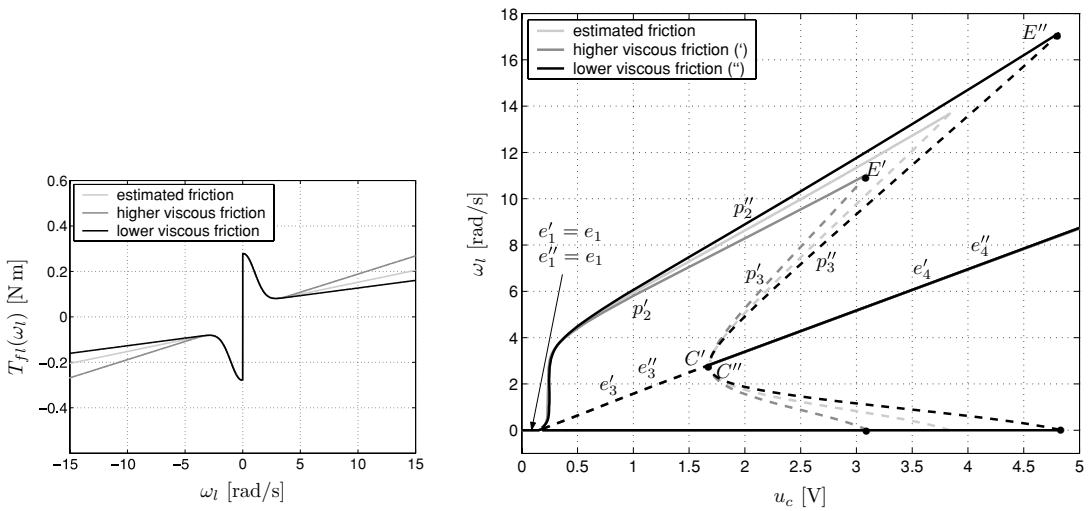

(a) Friction torques for various viscous friction levels.

(b) Bifurcation diagrams.

Fig. 11 Friction torques for various viscous friction levels and related bifurcation diagrams

situation, the viscous friction level is lower (black line in the same figure) than in the nominal friction torque (light-grey line). The related bifurcation diagrams and the bifurcation diagram for the estimated friction model of the set-up are shown in Fig. 11(b). When we compare the obtained bifurcation diagrams the following can be concluded:

- Equilibrium branches e_1, e_1' and e_1'' are identical for all friction situations.
- The Hopf bifurcation points C, C' and C'' occur for (nearly) identical constant input voltages for all friction situations.
- If the viscous friction level is lower, then the fold bifurcation point E'' appears for higher constant input voltages; i.e. in such cases torsional vibrations can appear for larger range of input voltages u_c (compare discontinuous fold bifurcation points E' and E'' in Fig. 11(b)). This can be explained in a similar fashion as we explained the influence of the negative damping level on the bifurcation diagram using the analysis of global stability properties of the equilibrium points performed in Section 4.1. Namely, for a lower viscous friction level, u_{g2} is higher (see expression (17) and Fig. 7(d)) and, therefore, the voltages at which no torsional vibrations can appear ($u_c > u_{g2}$) are higher ($u_{g2}' = 8.8290$ V for the friction plotted by the dark-grey line and $u_{g2}'' = 18.3156$ V for the friction plotted by the black line). Indeed, Fig. 11 shows that if the range of angular velocities defined by $\omega_l \in [\omega_1, \omega_{g2}]$ decreases (increases), due to a higher (lower) viscous friction level, then the region (in terms of input voltages) of co-existence decreases (increases).
- In Fig. 11(b), we observe that a lower viscous friction level causes higher amplitudes of the torsional vibrations in the system. Namely, when the viscous friction level is lower, then the friction is also lower (see Fig. 11(a)); hence, the dissipated energy is lower and the amplitude of torsional vibrations is larger.

5. Experiments

In this section, the steady-state behaviour (for constant input voltages) of the experimental drill-string system is studied and compared to the model-based results. In Section 5.1, the bifurcation diagram of the estimated (nominal) case is compared to an experimentally constructed bifurcation diagram. In analogy to Section 4.3, in Section 5.2 the dependency of the steady-state behaviour on the friction characteristics is studied experimentally.

5.1. Bifurcation diagram (nominal case)

In order to check the validity of the obtained model of the drill-string set-up when ondina oil 68 is used as a lubrication fluid and a 20.5 N normal force is applied at the brake, experimental results are compared with the

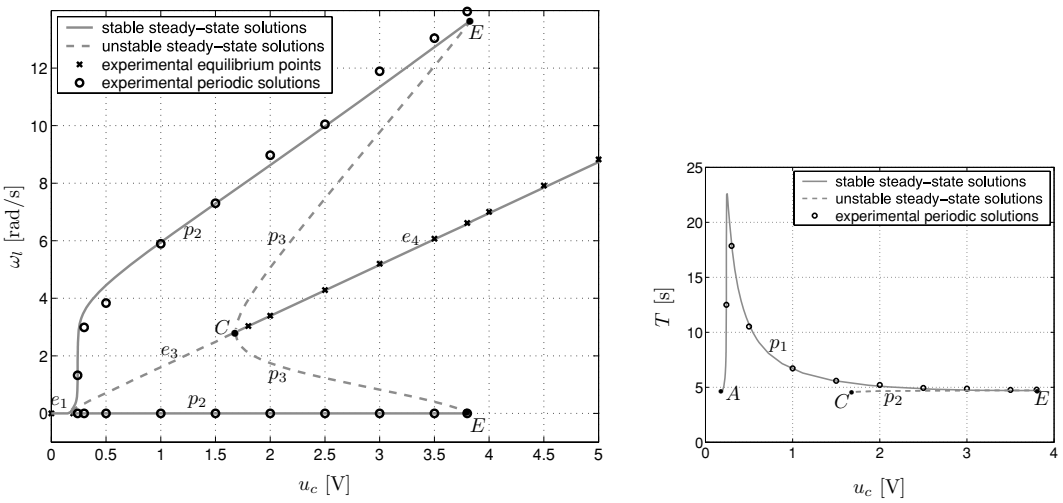

(a) Bifurcation diagram. (b) Period time of the periodic solutions.

Fig. 12 Comparison of the simulated and experimental bifurcation diagram

model-based results. As already mentioned earlier, the predictive quality of the estimated model in steady-state is of great interest. Therefore, when a constant voltage is applied at the input of the set-up, each experiment lasted long enough to guarantee that all transient effects have disappeared and the last part of the measurement signals are recorded.

The same type of bifurcation diagram, as shown in Fig. 9, is constructed experimentally. In order to construct such experimental bifurcation diagram, a range of constant input voltages are applied to the set-up. When no torsional vibrations are observed (the system is in equilibrium), the mean value of the recorded angular velocity is computed and obtained data are plotted using the symbol "**x**". When torsional vibrations are observed at the lower disc, the mean value of local maxima and the mean value of local minima of the vibrations are computed. Then, these experimentally obtained data are plotted using the symbol "**o**". Such experimental results, together with the bifurcation diagram obtained by a numerical analysis of the estimated model, are shown in Fig. 12(a). Moreover, when torsional vibrations are observed in the set-up, the period time T of the vibrations is determined as well. In Fig. 12(b) such experimental results are compared to the period time of the numerically obtained limit cycles. The results, shown in Fig. 12, illustrate the predictive quality of the obtained model.

Both in the numerical and the experimental bifurcation diagram we notice qualitatively different behaviour of the system when the constant input voltage is changed:

- For very low input voltages, the system is in the sticking phase.
- If the input voltage is increased, the system enters the region where only torsional vibrations (i.e. stable limit cycles) appear.
- If the input voltage is even higher, then the input voltage is in the region where torsional vibrations (stable limit cycles) and constant angular velocity at the lower disc (stable equilibrium points) co-exist in the set-up.
- If the input voltage is high enough ($u_c > 3.8$ V), the system enters the region where no torsional vibrations can appear in the system in steady-state.

In order to show that the experimental behaviour indeed matches well with the model behaviour, a comparison between the experimentally and numerically obtained time-series is provided in Fig. 13. In this figure, the experimental angular velocity (solid black line) and the angular velocity obtained using the estimated model (dashed grey line) in steady-state are shown for different constant input voltages. Namely, signals depicted in Figs. 13(a–c) represent stick-slip limit-cycling (torsional vibrations) and Fig. 13(d) represents an equilibrium point. Clearly, the combination of Fig. 13(c) and (d) confirms that in the experiments a region exists for which both stable equilibria and stable limit cycles exist. From the comparison between simulation

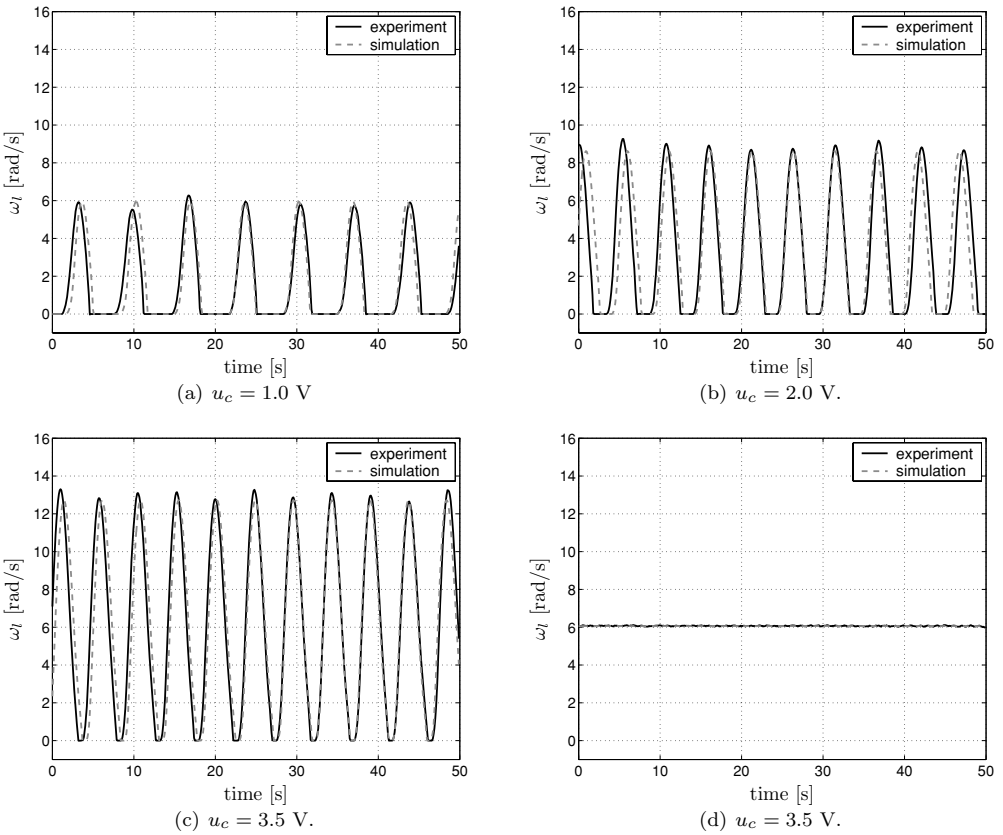

(a) $u_c = 1.0$ V (b) $u_c = 2.0$ V. (c) $u_c = 3.5$ V. (d) $u_c = 3.5$ V.

Fig. 13 Experimental and simulated angular velocity at the lower disc for various constant input voltages and various initial conditions

and experimental results, it can be concluded that with the suggested model the steady-state behaviour of the set-up is modelled accurately.

5.2. Changes in the friction characteristics

In Section 4.3, we have analyzed how various changes in the friction characteristics can influence torsional vibrations in drill-string systems. Here, we investigate the way in which various friction conditions influence torsional vibrations in the experimental set-up.

5.2.1. Changes in the applied normal force

In order to analyze how changes in the normal force, which is applied to the brake, influence the steady-state behaviour of the set-up, we subsequently apply a 18 N and a 12.2 N normal force to the brake. Next, the parameters of the model of the obtained friction torques are estimated, using a similar identification procedure used to identify the nominal model, see Section 3. The obtained models are validated and numerical and experimental bifurcation diagrams are constructed for both normal force levels. The estimated friction models $T_{fl}(\omega_l)$ are shown in Fig. 14. The related bifurcation diagrams are shown in Fig. 15.

When a lower normal force is applied to the brake, the static friction level is lower, the sticking region decreases and the lower disc starts to rotate for lower input voltages. Furthermore, for lower normal force levels, the separation process between the contacting surfaces (brake disc and the brake blocks) and, therefore, the full fluid lubrication regime occur for lower velocities (different friction regimes are depicted schematically in Fig. 16). Moreover, in Section 4.1 we have concluded that the position of the second Hopf bifurcation point is determined by the point on the friction curve $T_{fl}(\omega_l)$ where the negative damping reaches the value

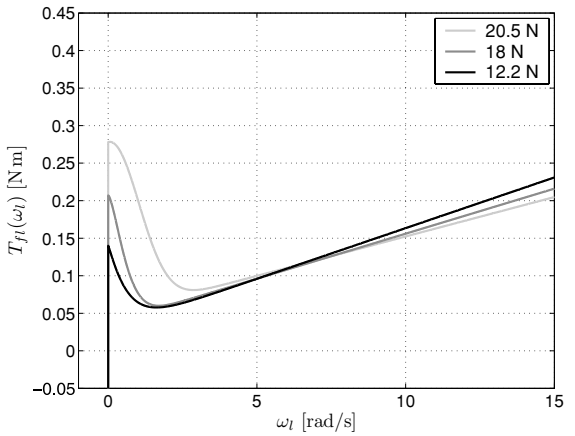

Fig. 14 Estimated friction models for the friction at the lower disc for various normal force levels applied at the brake

$d_{\min}$ ($\omega_{eq} = \omega_{h2}$). This, in fact, corresponds to the point where the full fluid lubrication appears (see Fig. 16). Consequently, for lower normal force levels, the Hopf bifurcation points C' and C'' in Fig. 15 appear for lower input voltages and the region, in which a constant velocity at the lower disc (a stable equilibrium) can appear, increases.

From Fig. 14, it can be seen that we estimate a higher viscous friction coefficient for a lower normal force level. Namely, when a lower normal force is applied, full fluid lubrication appears at the lower angular velocities. Moreover, for higher normal forces (and u_c high enough) the system is closer to the transition between the partial and full fluid lubrication regime than when the normal force is lower. Consequently, in the range of input voltages which can be applied to the system, this effect is modelled with a lower viscous friction for higher normal forces. However, if normal forces are low enough, the effects which cause the negative damping in friction disappear and torsional vibrations in the drill-string system also disappear. In the considered experimental drill-string set-up torsional vibrations disappear when the normal force is smaller than 7.8 N. An important observation is that the normal force influences the friction characteristics in a rather complex way, which can be explained using the friction regimes in Fig. 16. By no means the normal force forms a mere scaling factor for the friction force.

Moreover, Figs. 14 and 15 indicate, on an experimental level, that if the range of angular velocities defined by $\omega_l \in [\omega_1, \omega_{g2}]$ decreases, in this case due to a decreasing normal force level, then the region (in terms of input voltages) of co-existence decreases (mainly due to the fact that the discontinuous fold bifurcation point E moves to lower constant input voltages).

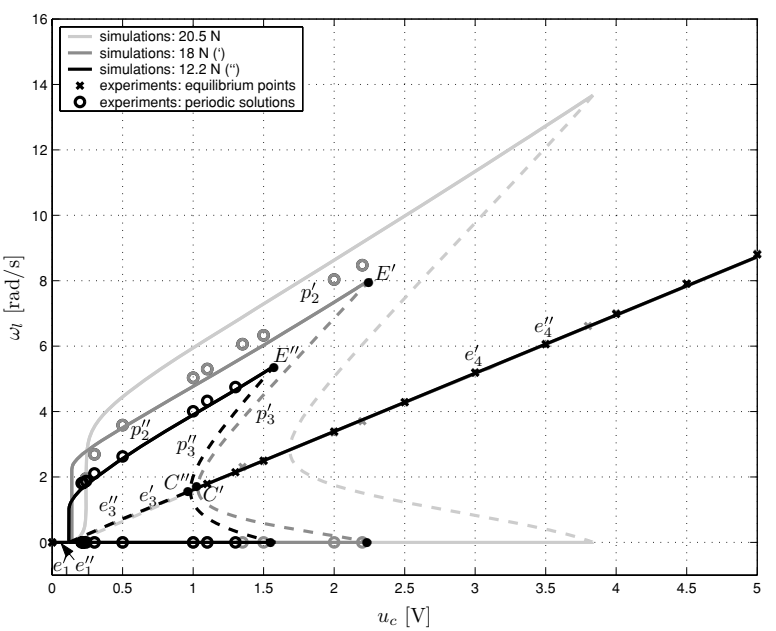

Fig. 15 Dependency of the bifurcation diagram on the normal force level

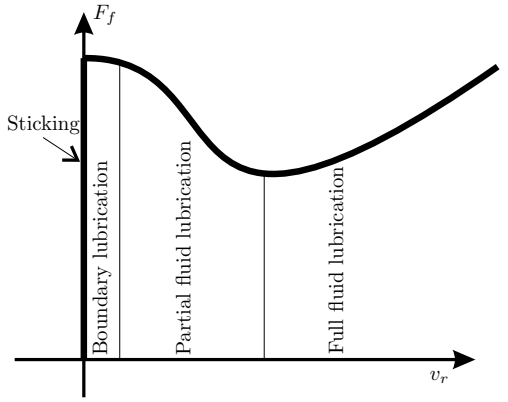

Fig. 16 Different regimes in the friction force

5.2.2. Temperature changes

The results, which are analyzed in Section 5.1, are obtained when the temperature in the laboratory, where the set-up is placed, is between 25 °C and 30 °C. The same kind of experimental results are collected when the temperature in the laboratory is between 17 °C and 22 °C, for the same normal force applied at the brake (20.5 N). The parameters of the obtained friction torque are estimated, the obtained model is validated and both the numerical and experimental bifurcation diagrams are constructed. The estimated friction torque at the lower part of the set-up is shown in Fig. 17(a). The related bifurcation diagrams are shown in Fig. 17(b).

When the temperature is lower, the viscosity of the oil becomes higher. With such oil, the separation between the contacting surfaces (brake disc and the brake blocks in the experimental set-up) and the full fluid lubrication process occurs for lower velocities. In Section 4.1, we have concluded that the position of the second Hopf bifurcation point is determined by the angular velocity ω_l for which the negative damping in $T_{fl}(\omega_l)$ reaches value $d_{\min}$, which corresponds to the point where full fluid lubrication appears (see Fig. 16). Consequently, the Hopf bifurcation point C', in Fig. 17(b), appears for lower input voltages than it does in the set-up when the temperature in the laboratory is higher.

Moreover, in Section 4.3 we also conclude that a higher viscous friction level causes the decrease of the amplitude of torsional vibrations and that the range of voltages in which torsional vibrations can appear is smaller (compare Fig. 11 with Fig. 17).

Finally, Fig. 17 indicates on an experimental level that if the range of angular velocities defined by $\omega_l \in [\omega_1, \omega_{g2}]$ decreases, in this case due to a lower temperature, then the region (in terms of input voltages) of co-existence decreases.

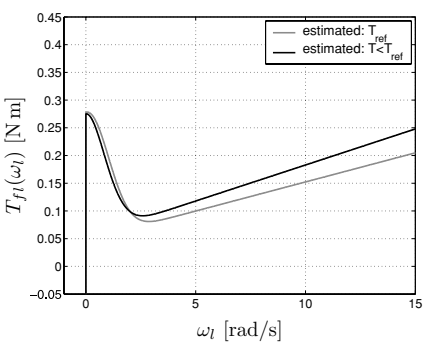

(a) Estimated friction model at the lower disc for various temperatures.

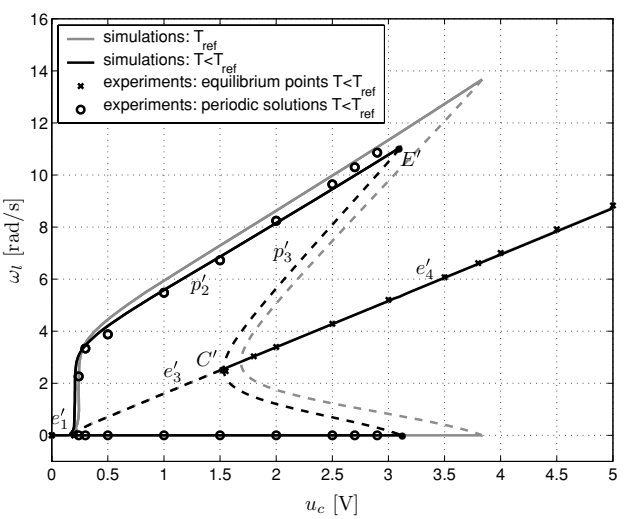

(b) Bifurcation diagrams.

Fig. 17 Dependency of the friction characteristics and the bifurcation diagram on temperature changes: $T \in [17\,^\circ\text{C}, 22\,^\circ\text{C}]$ and $T_{ref} \in [25\,^\circ\text{C}, 30\,^\circ\text{C}]$

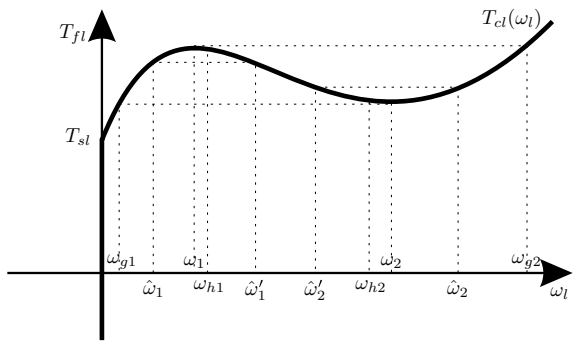

Fig. 18 A humped friction model as shown in Fig. 7(a)

6. Conclusions

In this paper, we investigate the way in which the occurrence and nature of friction-induced limit cycling in flexible mechanical systems (e.g. a drill-string system) depends on essential friction characteristics. This study is performed on the level of a theoretical stability analysis and both model-based and experimental bifurcation analyses. The striking similarity of these model-based and experimental results confirms the quality of the model. The main conclusion, which is based on theoretical, numerical and experimental results, is that a subtle interplay of negative damping characteristics at low velocities and viscous friction at higher velocities determines the occurrence and nature of the friction-induced limit cycling and the range of parameters for which these limit cycles sustain. Moreover, results on all levels confirm that discontinuous bifurcations play a crucial role in the creation and destruction of these limit cycles.

The way in which such friction characteristics are influenced by physical conditions such as temperature and normal forces on the frictional contact is studied experimentally. An important observation is that the normal force in the frictional contact influences the friction force in a rather complex way and can induce a higher negative damping level (for higher normal forces), which in turn can give rise to limit cycles of higher amplitudes for a larger range of parameters.

It should be noted that the configuration of the experimental set-up (two masses, coupled by a flexibility, of which one is subject to friction and the other is driven by an actuator) can be recognised in many other mechanical systems, in which friction deteriorates the system performance by the induction of vibrations. In this context, one can think of printers, pick and place machines, industrial and domestic robots, simple earthquake models, accurate mirror positioning systems on satellites and many more. Finally, the insight gained by this work could very well be used to steer research on controller design for such systems aiming at the avoidance of friction-induced limit cycling.

Appendix A: Non-local asymptotic stability of equilibria

In this appendix, the (non-local) stability properties of the equilibria of system (1) will be investigated. Here, we will address the stability properties of the equilibria for the case of a humped friction model for the friction at the lower disc as given in Fig. 7(a). Based on that analysis we will also be able to draw conclusions for the case when the friction at the lower disc is as depicted in Figs. 6(a), 7(c) and 8(a).

Let us assess the stability properties of the *isolated* equilibria using the candidate Lyapunov function V given by (12). The time-derivative of V obeys (13). Note that, for the friction model for the friction at the upper disc, the incremental sector condition (14) is satisfied. When $T_{fl}(\omega_l)$ is represented by a humped friction model, as shown in Fig. 7(a), then the incremental sector condition (15) can be satisfied in the neighborhood of an equilibrium point only when

$$u_c \in (u_{\mathcal{E}},\, u_1) \cup (u_2,\, \infty), \tag{19}$$

where $u_{\mathcal{E}}$ is defined by (7) and

$$u_1 = \frac{T_{cu}(\omega_1) + T_{cl}(\omega_1)}{k_m},\ u_2 = \frac{T_{cu}(\omega_2) + T_{cl}(\omega_2)}{k_m}, \tag{20}$$

where ω_1 and ω_2 are defined by (18) (see also Fig. 18). In other words, $\dot{V}(\boldsymbol{x},\, \boldsymbol{x}_{eq})$ can be shown to be negative semidefinite, at least in a neighborhood of $\boldsymbol{x}_{eq}$, when $\boldsymbol{x}_{eq}$ is such that

$$\left.\frac{\mathrm{d}T_{cl}}{\mathrm{d}\omega_l}\right|_{\omega_l=\omega_{eq}} > 0. \tag{21}$$

As a consequence, stability is guaranteed for equilibrium points satisfying (19). Let us now address the issue of *asymptotic* stability.

We first focus on a range of input voltages for which *global* asymptotic stability can be shown. Note that when the input voltage u_c satisfies the condition $u_c \in (0, u_{g1}) \cup (u_{g2}, \infty)$, with u_{g1} and u_{g2} defined by (17) and ω_{g1} and ω_{g2} visualised in Fig. 18, then the related equilibrium point $\boldsymbol{x}_{eq}$ is such that condition (15) is satisfied for all $\boldsymbol{x} \in \mathbb{R}^3$; consequently, $\dot{V}(\boldsymbol{x},\ \boldsymbol{x}_{eq}) \leq 0$ for all $\boldsymbol{x} \in \mathbb{R}^3$. For such equilibria, it can be concluded that $\dot{V}(\boldsymbol{x},\ \boldsymbol{x}_{eq}) = 0$ for $\boldsymbol{x} \in \mathcal{L}$, with

$$\mathcal{L} = \{\boldsymbol{x} \in \mathbb{R}^3 \ \mid \omega_u = \omega_{eq},\ \dot{\alpha} = 0\}. \tag{22}$$

If $\boldsymbol{x} \in \mathcal{L}$, then $\omega_u = \omega_{eq} = \text{const}$ and $\dot{\alpha} = 0$. Consequently, for an invariant subset of $\mathcal{L}$ it should hold that $\dot{\omega}_u = \ddot{\alpha} = 0$. If we substitute this in the equations of motion (1) of the system, then the obtained equations can only be satisfied in the equilibrium point. This leads to the conclusion that such an equilibrium point $\boldsymbol{x}_{eq}$ represents the largest invariant set on $\mathcal{L}$. The application of LaSalle's invariance principle now proves that such equilibrium points are attractive and the whole state space $\mathbb{R}^3$ represents the region of attraction. Therefore, since we proved that every equilibrium point is stable and globally attractive, we can conclude that all those equilibria are globally asymptotically stable. We illustrate this fact graphically in Fig. 7(b).

In the range of input voltages $u_c \in (u_{g1}, u_1) \cup (u_2, u_{g2})$ global stability can not be guaranteed. Let us now consider such an equilibrium for $u_c = \hat{u}_2$ (with $\hat{u}_2 \in (u_2, u_{g2})$), given by

$$\hat{u}_2 = \frac{T_{cu}(\hat{\omega}_2) + T_{cl}(\hat{\omega}_2)}{k_m}, \tag{23}$$

see Fig. 18. For such an equilibrium, $\dot{V}(\boldsymbol{x},\ \boldsymbol{x}_{eq}) \leq 0,\ \forall \boldsymbol{x} \in \mathcal{B}_2$, with

$$\mathcal{B}_2 = \{\boldsymbol{x} \in \mathbb{R}^3 \mid \omega_l \in [\hat{\omega}_2', \hat{\omega}_2]\}, \tag{24}$$

where $\hat{\omega}_2'$ is such that $T_{fl}(\omega_l) \leq T_{fl}(\hat{\omega}_2)$, for all ω_l in the connected set $[\hat{\omega}_2', \hat{\omega}_2]$. Moreover, we define a set $\mathbf{x} \in \bar{\mathcal{L}}$, on which $\dot{V}(\boldsymbol{x},\ \boldsymbol{x}_{eq}) = 0$, by

$$\bar{\mathcal{L}} = \{\boldsymbol{x} \in \mathcal{B}_2 \mid \omega_u = \omega_{eq},\ \dot{\alpha} = 0\}. \tag{25}$$

Again we can conclude that such equilibrium points $\boldsymbol{x}_{eq}$ represents the largest invariant set on $\bar{\mathcal{L}}$ and application of LaSalle's invariance principle now proves that such equilibrium points are (at least locally) attractive. Therefore, since we proved that every equilibrium point is stable and locally attractive, we can conclude that all those equilibria are locally asymptotically stable. An estimate of the region of attraction of $\boldsymbol{x}_{eq}$ is given by:

$$\begin{aligned}\mathcal{I}_{\rho_{\max}} &= \{\boldsymbol{x} \in \mathbb{R}^3 \ \mid V(\boldsymbol{x},\ \boldsymbol{x}_{eq}) < \rho_{\max}\},\ \text{with } \rho_{\max} \\ &= \max_{\mathcal{I}_\rho \subset \mathcal{B}_2} \rho,\end{aligned} \tag{26}$$

with

$$\mathcal{I}_\rho = \{\boldsymbol{x} \in \mathbb{R}^3 \ \mid V(\boldsymbol{x},\ \boldsymbol{x}_{eq}) < \rho\}. \tag{27}$$

Consequently, if $\hat{u}_2$ is closer to u_2, defined by (20), then the set $\mathcal{I}_{\rho_{\max}}$ is smaller and therefore the estimate of the basin of attraction of the equilibrium point for $u_c = \hat{u}_2$ is also smaller, see Fig. 7(b). A similar reasoning can be adopted for equilibria, for input voltages $u_c = \hat{u}_1$, with $\hat{u}_1 \in (u_{g1}, u_1)$. This concludes the proof of the (non-local) stability properties of the isolated equilibria in case of a friction model as depicted in Fig. 7(a).

For the stability proof of the equilibrium set, which is based on the same candidate Lyapunov function, we refer to [23, 24]. Based on the results therein we conclude that for the friction model presented in Fig. 7(a), the equilibrium set is globally asymptotically stable. The entire stability analysis presented above yields the stability of all equilibria as depicted schematically in Fig. 7(b).

For a monotonically increasing friction model $T_{fl}(\omega_l)$, as in Fig. 6(a), the incremental sector condition (15) is satisfied globally for all equilibria. Hence global asymptotic stability can be proven, using similar reasoning as above, for all isolated equilibria and equilibrium sets, see Fig. 6(b).

Now, let us consider the humped friction model shown in Fig. 7(c). The only differences between the stability properties of the equilibria for this friction model and those for the friction model shown in Fig. 7(a) are that the isolated equilibria can only be proven to be globally asymptotically stable for $u_c > u_{g2}$ and that the equilibrium set can only be proven to be locally asymptotically stable [24]. This leads to the stability results as depicted in Fig. 7(d).

Finally, the stability results for the equilibria for a friction model as shown in Fig. 8(a) differs from those for the friction model in Fig. 7(c) in the sense that the

asymptotic stability of the equilibrium set as a whole can not be shown, however almost all points of the equilibrium set (except the boundary points of the equilibrium set) are Lyapunov stable [24]. This degradation of the stability properties is directly related to the fact that negative damping occurs for infinitesimally small ω_l in $T_{fl}(\omega_l)$.

References

1. Brett, J.F.: Genesis of torsional drillstring vibrations. SPE Drill. Eng. **7**(3), 168–174 (1992)
2. Leine, R.I., van Campen, D.H., Keultjes, W.J.G.: Stick-slip whirl interaction in drillstring dynamics. ASME J. Vib. Acoust. **124**, 209–220 (2002)
3. Kreuzer, E., Kust, O.: Analyse selbsterregter drehschwingugnen in torsionsstäben. ZAMM – J. Appl. Math. Mech. / Zeitschrift fuer Angewandte Mathematik und Mechanik **76**(10), 547–557 (1996a)
4. Pfeiffer, F., Hajek, M.: Slip-stick motions of turbine blade damp. Philos. Transl. R. Soc. Lond. A **338**(9), 503–517 (1992)
5. Hensen, R.H.A.: Controlled Mechanical Systems with Friction. Ph.D. thesis, Endhoven University of Technology, The Netherlands (2002)
6. Cataldi, E., Glocker, Ch.: Curve squealing of railroad vehicles. In: Proceedings of the 5th EUROMECH Nonlinear Oscillations Conference, Eindhoven, The Netherlands (2005)
7. Cunningham, R.A.: Analysis of downhole measurements of drill string forces and motions. ASME J. Eng. Ind. **90**, 208–216 (1968)
8. Jansen, J.D., van den Steen, L.: Active damping of self-excited torsional vibrations in oil well drillstrings. J. Sound Vib. **179**(4), 647–668 (1995)
9. Van den Steen, L.: Suppressing Stick-Slip-Induced Drillstring Oscillations: a Hyper Stability Approach. Ph.D. thesis, University of Twente (1997)
10. Richard, T., Germay, C., Detournay, E.: Self-excited stick-slip oscillations of drill bits. C. R. Mec. **332**, 619–626 (2004)
11. Brockley, C.A., Cameron, R., Potter, A.F.: Friction-induced vibrations. ASME J. Lubr. Technol. **89**, 101–108 (1967)
12. Brockley, C.A., Ko, P.L.: Quasi-harmonic friction-induced vibrations. ASME J. Lubr. Technol. **92**, 550–556 (1970)
13. Ibrahim, R.A.: Friction-induced vibration, chatter, squeal, and chaos: mechanics of contact and friction. Appl. Mech. Rev.: ASME **47**(7), 209–226 (1994a)
14. Ibrahim, R.A.: Friction-induced vibration, chatter, squeal, and chaos: dynamics and modeling. Appl. Mech. Rev.: ASME **47**(7), 227–253 (1994b)
15. Popp, K., Stelter, P.: Stick-slip vibrations and chaos. Philos. Trans. R. Soc. Lond. **332**, 89–105 (1990)
16. Popp, K., Rudolph, M., Kröger, M., Lindner, M.: Mechanisms to generate and to avoid friction induced vibrations. VDI-Berichte 1736, VDI-Verlag Dsseldorf 2002, 1–15 (2002)
17. Krauter, A.I.: Generation of squeal/chatter in water-lubricated elastomeric bearings. ASME J. Lubr. Technol. **103**, 406–413 (1981)
18. Hensen, R.H.A., van de Molengraft, M.J.G., Steinbuch, M.: Friction induced hunting limit cycles: an event mapping approach, In: Proceeding of the 2002 American Control Conference, Anchorage, AK (2002)
19. Putra, D., Nijmeijer, H.: Limit cycling in an observer-based controlled system with friction: numerical analysis and experimental validation. Int. J. Bifurcation Chaos **14**(9), 3083–3093 (2004)
20. Olsson, H., Åström, K.J.: Friction generated limit cycles. In: Proceeding of the 1996 IEEE Conference on Control Applications, Dearborn, MI, (1996)
21. Olsson, H., Åström, K.J.: Friction generated limit cycles. IEEE Conf. Control Syst. Technol. **9**(4), 629–636 (2001)
22. Van de Wouw, N., Mallon, N.J., Nijmeijer, H.: Friction compensation in a controlled one-link robot using a reduced-order observer, In: Proceedings of 6th IFAC Symposium on Nonlinear Control Systems (NOLCOS), (2004)
23. Mihajlović, N., Van Veggel, A.A., Van de Wouw, N., Nijmeijer, H.: Analysis of friction-induced limit cycling in an experimental drill-string set-up. ASME J. Dyn. Syst. Meas. Control **126**(4), 709–720 (2004)
24. Mihajlovic, N.: Torsional and Lateral Vibrations in Flexible Rotor Systems with Friction. Ph.D. thesis, Eindhoven University of Technology, The Netherlands, (2005)
25. Mihajlović, N., Van Veggel, A.A., Van de Wouw, N., Nijmeijer, H.: Friction-induced torsional vibrations in an experimental drill-string system, In: Proceedings of the 23rd IASTED International conference on Modelling, Identification, and Control, Grindelwald, Switzerland (2004)
26. Ascher, U.M., Mattheij, R.M.M., Russell, D.R.: Numerical solution of boundary value problems for ordinary differential equations. SIAM, Philadelphia, (1995)
27. Parker, T.S., Chua, L.O.: Practical Numerical Algorithms for Chaotic Systems. Springer-Verlag, New York (1989)
28. Leine, R.I., Nijmeijer, H.: Dynamics and Bifurcations of Non-Smooth Mechanical Systems. Springer, Berlin (2004)
29. Leine, R., Van Campen, D., van de Vrande, B.: Bifurcations in nonlinear discontinuous systems. Nonlinear Dyn. **23**, 105–164 (2000)
30. Galvanetto, U., Bishop, S.: Dynamics of a simple damped oscillator undergoing stick-slip vibrations. Meccanica **34**(5), 337–347 (1999)